

## **Strong oblique shock waves in granular free-surface flows**

CUI, Xinjun <<http://orcid.org/0000-0003-0581-3468>>

Available from Sheffield Hallam University Research Archive (SHURA) at:

<http://shura.shu.ac.uk/29151/>

---

This document is the author deposited version. You are advised to consult the publisher's version if you wish to cite from it.

### **Published version**

CUI, Xinjun (2021). Strong oblique shock waves in granular free-surface flows. *Physics of Fluids*, 33 (8), 083302-083302.

---

### **Copyright and re-use policy**

See <http://shura.shu.ac.uk/information.html>

## Strong oblique shock waves in granular free-surface flows

X. Cui\*

*Aerospace Engineering, Department of Engineering & Mathematics  
Sheffield Hallam University, Sheffield S1 1WB, UK.*

(Dated: July 12, 2021)

Strong oblique shock waves of granular flow are a steady-state solution formed when a granular free-surface flow deflects around a wedge-shaped obstacle at a supercritical speed, but they do not usually occur because their formation requires specific conditions to be satisfied downstream of the shock wave. This paper discusses the method of generating the strong oblique shock wave in laboratory experiment and numerical simulation. The experiment is conducted on a plexiglass chute inclined at an angle to the horizontal, in which a dry granular material is released from a hopper at the top of the chute to form a channelized flow that passes a wedge at a downslope location. In order to generate a strong oblique shock wave, a second gate is established at the downstream of the wedge to control the material to flow out only at the designed time and height. Such a granular flowing process is simulated with a depth-averaged granular flow model, where the above two-gate system is mirrored into the inlet and outlet boundaries, respectively. The formation of the strong oblique shock is investigated through the transient solution of the flow field, and a good agreement is observed between the experiment and the simulation. Then, the steady-state solution of the interaction between the weak and strong oblique shocks is analysed in the experiment and simulation. This result can be regarded as the third solution of granular shock because it can be formed by just changing the opening time of the second gate. With the dramatic change in flow thickness and velocity across the strong oblique shock, the bulk inertial number, used to quantify the rheological relation of granular materials, becomes extremely small, but it does not seem to affect the behaviour of the flow discussed in this paper.

PACS numbers: Valid PACS appear here

### I. INTRODUCTION

Granular free-surface flows driven by gravity are commonly seen in industrial (e.g. food, mining, chemical or pharmaceutical) and natural (e.g. volcanic, mud-slide or snow-avalanche) processes. An important phenomenon often observed in such processes is that when granular materials travel faster than the speed of sound and are deflected by obstacles, shock waves are generated. Such shock waves bear many similarities with the hydraulic jumps of water flows (see,<sup>1,2,3</sup>). Since granular flows usually exhibit a weak scale dependence, laboratory experiments can be used to gain important insight into these processes. Savage (1979)<sup>4</sup> studied a granular avalanche moving down an inclined chute and observed a granular shock wave being generated when the flow was stopped by a downstream splitter. Savage & Hutter (1989)<sup>5</sup> modelled the governing equations as a shallow-water type for granular flows by incorporating a Mohr-Coulomb law for the basal friction. Hutter *et al.* (1993)<sup>6</sup> later introduced a “jump” term into the basal friction law to reflect the discontinuous change across shock waves, and Wieland *et al.* (1999)<sup>7</sup> used this relation to simulate a granular avalanche moving on a curved bed. When studying the flow around various obstacles, Gray *et al.* (2003) showed that the simple Coulomb friction law still works well in the granular shock simulation.

The attempts to establish a more complex rheological relationship show that as the flow of granular materials becomes more complicated, the corresponding rheological law may need to be more complex to reflect the be-

haviours of the flow as well. Pouliquen (1999)<sup>9</sup> scaled the mean flow velocity of his measurement according to the minimum thickness that varies with the inclination angle of the slope, and proposed an empirical expression for the dynamic friction coefficient,  $\mu$ , as a function of the flow velocity  $\bar{u}$  and thickness  $h$ , followed by further improvements<sup>10,11</sup>. By investigating the viscoplastic behaviour of the gravitationally-driven granular flow bounded between two parallel rough side walls, a French research group (2004)<sup>12</sup> modelled the rheological behaviour of  $\mu$  according to a dimensionless inertial number,

$$I = \frac{\dot{\gamma}_w \tilde{d}}{\sqrt{P/\rho}}, \quad (1)$$

where  $\dot{\gamma}_w$  represents a mean shear rate,  $P$  is the normal hydrostatic pressure,  $\rho$  the density of the grain, and  $\tilde{d}$  the diameter of the grain. The introduction of the inertia number has brought great convenience to the description of the law of basal friction, so the form of  $\mu(I)$  has since become a commonly-used method of expressing the rheological law of granular materials, e.g.,<sup>13–17</sup>. In the mean time, the validity of the  $\mu(I)$ -rheology has been examined for a wider range of parameters by Holyoake & McElwaine (2012)<sup>18</sup>, where they tested a sand flow down a steep chute for both flat and bumpy basal conditions over much deeper slope angles, and concluded that the  $\mu(I)$ -rheology does not fully capture the accelerating dynamics or the transverse velocity profile on the bumpy base. Gray & Edwards (2014)<sup>19</sup> incorporated the  $\mu(I)$ -rheology into the depth-averaged granular flow

model and showed that the rheology cannot be used outside the range of angles where steady-uniform flows develop. The well-posed and ill-posed problem of the  $\mu(I)$ -rheology was addressed by Barker *et al.* (2015)<sup>20</sup>, and they showed that the  $\mu(I)$  representation works well for intermediate values of  $I$ , but becomes ill-posed when the inertial number becomes high or low. By considering the stretching of the convective Kelvin wave vector in basal flows, the stability of the  $\mu(I)$ -rheology was further studied for planar simple shearing and pure shearing flows<sup>21</sup>. With the advance of computing technology, meanwhile, the discrete element method (DEM) has become popular on understanding the rheological relations of granular material in recent years. Examples may include the numerical modelling of frictional ellipses<sup>22,23</sup>, DEM simulation of rod-like particles<sup>24</sup> and binary granular particles of different shapes<sup>25</sup>, and DEM modelling of rapid granular flows on inclines<sup>26</sup>. Above all, a more complex rheological law of granular material makes it possible to run simulations based on more complicated models<sup>27,28</sup>, and the study on the granular shock waves may provide a unique approach to understand the underlying rheology of granular materials due to the dramatic change in flow properties across the shock wave.

Tai *et al.* (2002)<sup>29</sup> used marker points to track the moving front of a granular shock in their chute-flow simulation. Pitman *et al.* (2003)<sup>30</sup> simulated the granular avalanches and landslides over a realistic terrain with the use of adaptive mesh. Following the work of Gray *et al.*<sup>8</sup>, Håkonardóttir and Hogg (2005)<sup>31</sup> further studied the granular flow around a wedge, and showed that the source terms, which are consisted of gravitational force and basal friction, can impose a substantial effect on the oblique shock angle. Amarouchene and Kelly (2006)<sup>32</sup> experimentally measured the speed of sound for the detached shock front in granular flows around square and circular obstacles. Gray & Cui (2007)<sup>33</sup> made a further study to the granular flow around wedge problem through numerical simulations and experiments, and formulated the oblique shock wave relation for granular flows. At the same time, Cui *et al.* (2007)<sup>34</sup> simulated the movement of a snow avalanche under the realistic topographic conditions at Flateyri, Iceland, and showed that an oblique shock was generated when the avalanche was deflected by a defensive dam. Other examples of granular shock studies may include granular jets and hydraulic jumps on an inclined plane<sup>35</sup>, bow shock waves around a circular cylinder<sup>36</sup>, travelling and steady shock waves over a smooth two-dimensional bump<sup>37</sup>. To have an overall picture about the studies of granular flow in recent years, readers may find the review written by Delannay *et al.*<sup>38</sup> helpful too, and this paper will focus on the strong oblique shock waves of granular flow.

According to the granular oblique shock relation<sup>33</sup>, there exist two solutions of oblique shock wave for a given incoming Froude number  $Fr_1$  if the wedge deflection angle,  $\theta$ , is smaller than its detachment angle  $\theta_{max}$ . For the convenience of discussion this relation has been re-

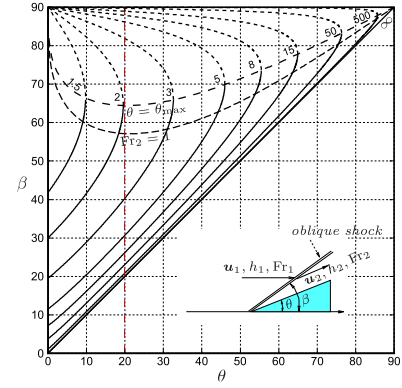


FIG. 1: The shock-deflection relation of granular flow for incoming Froude numbers  $Fr_1 = 1.5, 2, 3, 5, 8, 15, 50, 500, \infty$ . The solid lines denote the solution of weak shock, the shorter-dashed lines denote the solution of strong shock, the dash-dot line represents the after-shock  $Fr_2 = 1$ , and the longer-dashed line represents the detachment angle  $\theta_{max}$ .

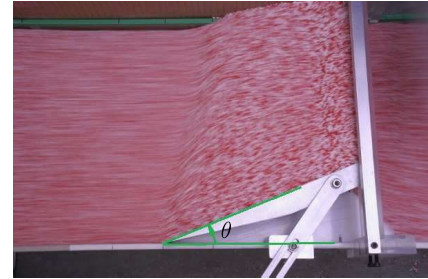


FIG. 2: An experimental photo showing a steady granular flow around an oblique wedge that has a deflection angle  $\theta = 20^\circ$ . The flow is driven down the slope by gravity, and a strong oblique shock wave is generated with the control of the outflow conditions through a downstream gate. The flow direction is oriented from left to right here.

produced in Fig. 1. From it, for example, if  $Fr_1 = 5$  and  $\theta = 20^\circ$ , one can get a smaller angle  $\beta_1 = 30.69^\circ$  corresponding to a weak oblique shock solution, and a larger angle  $\beta_2 = 86.15^\circ$  corresponding to a strong oblique shock solution, for  $\theta_{max} = 45.98^\circ$ . Usually weak oblique shock waves are favored to occur in most of natural granular flows when moving at supersonic speed ( $Fr_1 > 1$ ), whilst the occurrence of strong oblique shock waves depends on specific conditions to be met at the downstream of the shock. Shown in Fig. 2 is an experiment result of a steady granular flow impacting an oblique wedge with  $\theta = 20^\circ$ . A granular material, 100's and 1000's sprinkles in red and white, is released from a hopper at the top of a chute inclined at  $38^\circ$  angle to the horizontal, and

flows, from left to right, down the chute. A strong oblique shock wave is generated in this experiment since the outflow conditions downstream the wedge are controlled by a designated gate shown in this figure.

This paper will first discuss the method of generating strong oblique shock waves through laboratory experiment and numerical simulation, and then discuss the time-dependent and steady-state solutions obtained in the experiment and simulation. Investigation will then be made to the steady-state interaction between weak and strong oblique shock waves. Since the flow characteristics change more drastically when passing through the strong oblique shock wave, its influence on the inertia number  $I$  will be analysed at the end.

## II. GOVERNING EQUATIONS AND COMPUTATIONAL METHOD

### A. Governing equations for granular free-surface flows

The constitutive relation of granular materials can be extremely complicated when internal properties due to collision, deformation, friction and lubrication are considered. However if a flow moves at a relatively fast speed, e.g. snow avalanches, such internal complexities can be often negligible, leaving only the basal friction and the gravitational force to be considered. By “fast-moving” here it means that the Froude number (equivalent to the Mach number in gasdynamics) of the flow,

$$\text{Fr} = |\bar{\mathbf{u}}|/\sqrt{gh \cos \zeta}, \quad (2)$$

is greater than 1, where  $|\bar{\mathbf{u}}|$  is the depth-averaged flow speed,  $h$  the flow thickness,  $\zeta$  the inclination angle of a slope, whereas  $\sqrt{gh \cos \zeta}$  represents the wave propagation speed of the flow, and the tilde notation represents a dimensional term. A granular free-surface flow can be treated as a shallow-water type since the depth of the flow in the normal direction is much smaller than its travelling distance along the slope, therefore flow variables such as velocity can be simplified as a bulk entity by a depth-averaged integration (Savage & Hutter 1989<sup>5</sup>). Early types of such models started to appear in 1960's and 70's when snow avalanches were studied<sup>39–41</sup>, later more complicated basal frictional relations were introduced to similar types of model (e.g.<sup>5,42–44</sup>).

The governing equations used in this paper are briefly explained as follows. Suppose the equations are set up in a fixed Cartesian coordinate system,  $Oxy$ , with the origin  $O$  being at the start of an avalanching flow, the  $x$ -axis following the downslope direction of the chute inclined at an angle  $\zeta$  to the horizontal, and the  $y$ -axis being in the cross-slope direction of the chute. With  $\bar{\mathbf{u}}$  and  $\bar{\mathbf{v}}$  being the components of the depth-averaged velocity  $\bar{\mathbf{u}}$  in  $x$ - and  $y$ -directions, respectively, one can have the governing equations in dimensionless form as follows

$$\begin{aligned} (h)_t + (h\bar{u})_x + (h\bar{v})_y &= 0, \\ (h\bar{u})_t + (h\bar{u}^2)_x + (h\bar{u}\bar{v})_y + (\tfrac{1}{2}h^2 \cos \zeta)_x &= hS^x, \\ (h\bar{v})_t + (h\bar{u}\bar{v})_x + (h\bar{v}^2)_y + (\tfrac{1}{2}h^2 \cos \zeta)_y &= hS^y, \end{aligned} \quad (3)$$

and the source terms of the right-hand side are

$$\begin{aligned} S^x &= \sin \zeta - \mu(\bar{u}/|\bar{\mathbf{u}}|)(\cos \zeta - \frac{\partial \zeta}{\partial x} \bar{u}^2) - \frac{\partial b}{\partial x} \cos \zeta, \\ S^y &= -\mu(\bar{v}/|\bar{\mathbf{u}}|)(\cos \zeta - \frac{\partial \zeta}{\partial x} \bar{u}^2) - \frac{\partial b}{\partial y} \cos \zeta, \end{aligned} \quad (4)$$

where  $\mu$  is the coefficient of friction,  $b$  is the height of the topography normal to the reference base,  $\zeta$  is allowed to vary in the  $x$ -direction for a possible topographical change of the basal surface. The Coulomb friction law is given by  $\mu = \tan \delta$ , with  $\delta$  being the basal friction angle. To obtain the non-dimensional form of (3), the following scalings have been applied: 1 unit of length is equal to 30 millimeters (denoted  $L$ ), 1 unit of time is equal to 0.0553 seconds (based on  $\sqrt{L/g}$ ), and 1 unit of velocity is equal to 0.5422 m/s (based on  $\sqrt{Lg}$ ), where  $g = 9.80 \text{ m/s}^2$ . Correspondingly, one can have another form of the Froude number,  $\text{Fr} = |\bar{\mathbf{u}}|/\sqrt{h \cos \zeta}$ .

If let  $S^x = S^y = 0$  and  $\partial/\partial t = 0$ , (3) can yield the following  $\theta - \beta - \text{Fr}$  relation<sup>33</sup>

$$\theta = \beta - \tan^{-1} \frac{1 + \sqrt{1 + 8\text{Fr}_1^2 \sin^2 \beta}}{2\text{Fr}_1^2 \sin 2\beta}, \quad (5)$$

which is plotted in Fig. 1.

Further introduce conservative variables,  $m = h\bar{u}$  and  $n = h\bar{v}$ , one can re-write (3) as

$$\frac{\partial U}{\partial t} + \frac{\partial E}{\partial x} + \frac{\partial F}{\partial y} = S, \quad (6)$$

where

$$\begin{aligned} U &= (h, m, n)^T, \\ E &= (m, m^2/h + h^2/2 \cos \zeta, mn/h)^T, \\ F &= (n, mn/h, n^2/h + h^2/2 \cos \zeta)^T, \\ S &= (0, hS^x, hS^y)^T, \end{aligned} \quad (7)$$

with the superscript “ $T$ ” denoting the transpose to a row vector.

### B. The computational method

The introduction of the TVD (total variation diminishing) concept by Harten (1983)<sup>45</sup> has since modernized the techniques of shock capturing in numerical simulations. This method makes it possible to highly resolve shock waves without causing numerical fluctuations across the discontinuity, and has been widely adopted



in gasdynamic simulations e.g. with the use of the upwind TVD method. By adopting a similar concept of TVD, Nessyahu & Tadmor (1990)<sup>46</sup> developed a second-order Non-Oscillatory Central (NOC) scheme based on the central difference of Lax-Friedrichs. Since then, a number of higher-order NOC schemes have been established (e.g.<sup>48–50,53</sup>).

Unlike the upwind TVD method, the central TVD scheme provides a simpler computational approach because the Riemann solver is no longer needed, but it has only been used in shock wave simulations on granular flows in recent years. Tai *et al.*<sup>29</sup> used a staggered NOC scheme to simulate the evolution of a one-dimensional parabolic cap. Gray *et al.*<sup>8</sup> used the same NOC scheme to simulate the granular avalanche past obstacles by incorporating the shape of obstacles as  $\partial b/\partial x$  and  $\partial b/\partial y$  (see, equation (4)). However, an NOC scheme without staggering the computational grid can be more easily implemented in simulations for the flow around an obstacle<sup>33,34,36,51</sup>, and are adopted in the present work too.

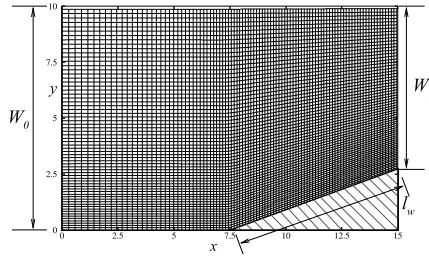


FIG. 3: An example of the computational grid, where the flow is oriented from left to right, and an oblique wedge is placed at the bottom right. The grid points here have been skipped to make it clearly visible in the domain.

Shown in Fig. 3 is the computational grid used for the simulation of the flow around a wedge with angle  $\theta = 20^\circ$ , where the  $x$ -direction covers a length of 15 dimensionless units in the downslope, and the  $y$ -direction covers a width of 10 units in the cross slope of the chute. Assume the flow is oriented from left to right in the domain, so the left boundary can be aligned at  $x = 0$  for a lateral width  $W_0 = 10$ . At this boundary, an initial (or inlet) condition is defined with a flow thickness  $h_0$  and a downslope velocity  $\bar{u}_0$ , for its cross-slope velocity  $\bar{v}_0 = 0$ . The right (or outlet) boundary is thus at  $x = 15$  in the domain, has a cross-slope width  $W_1$ , where  $W_1 = W_0 - l_w \sin \theta$ , with  $l_w$  being the length of the wedge. Other boundary conditions are given as follows: a symmetric condition is given to the bottom boundary up to the leading edge, then a slip wall condition to the wall surface of the wedge, and a far field condition is given to the top boundary to allow the free propagation of the shock wave. In order to properly generate the strong oblique shock wave, the

outlet condition in the simulation needs to be determined according to the conservation of mass flux as follows

$$\int_0^{W_0} h_0 \bar{u}_0 dy = \int_0^{W_1} h_1 \bar{u}_1 dy = h_0 \bar{u}_0 W_0, \quad (8)$$

where  $h_0$  and  $h_1$  correspond to the inlet and outlet flow thicknesses, respectively, and the term  $\bar{u}$  represents the resultant velocity for  $\bar{u}$  and  $\bar{v}$ . Since the flow at the inlet is one-dimensional and uniform, one can let  $\bar{u}_0 = \bar{u}_0$ , it then gives a constant product  $h_0 \bar{u}_0 W_0$  in equation (8). The detail of determining the outlet conditions will be explained later in Section III B.

For the finite difference method used here, it is convenient to use a body-fitted coordinate system, say,  $O'\xi\eta$ , in the computation domain, with the  $\xi$ -axis following the tangent along the wedge surface and the  $\eta$ -axis normal to  $\xi$  by pointing outward. Therefore, the governing equation (6) needs to be transformed into the computational domain through

$$\begin{aligned} \xi &= \xi(x, y), \\ \eta &= \eta(x, y), \\ \tau &= t, \end{aligned} \quad (9)$$

to give (e.g.<sup>52</sup>)

$$\frac{\partial \hat{U}}{\partial \tau} + \frac{\partial \hat{E}}{\partial \xi} + \frac{\partial \hat{F}}{\partial \eta} = \hat{S}, \quad (10)$$

where

$$\begin{aligned} \hat{U} &= J^{-1}U, \\ \hat{E} &= J^{-1}(\xi_x E + \xi_y F), \\ \hat{F} &= J^{-1}(\eta_x E + \eta_y F), \\ \hat{S} &= (0, J^{-1}hS^x, J^{-1}hS^y)^T. \end{aligned} \quad (11)$$

In these relations, the Jacobian coefficient  $J$  can be obtained by

$$J = \xi_x \eta_y - \xi_y \eta_x = (x_\xi y_\eta - x_\eta y_\xi)^{-1}, \quad (12)$$

where the terms  $\xi_x$ ,  $\xi_y$ ,  $\eta_x$  and  $\eta_y$  are coordinate derivatives with respect to the subscripted axes  $x$  or  $y$ . Note also that the physical velocity components  $(\bar{u}, \bar{v})$  are associated with  $(\hat{u}, \hat{v})$  in the computational domain by

$$\begin{pmatrix} \hat{u} \\ \hat{v} \end{pmatrix} = \begin{pmatrix} \xi_x & \xi_y \\ \eta_x & \eta_y \end{pmatrix} \begin{pmatrix} \bar{u} \\ \bar{v} \end{pmatrix}. \quad (13)$$

If denote a grid point with a discrete coordinate  $(j, l)$ , with  $j$  representing the  $\xi$  dependence and  $l$  the  $\eta$  dependence, an explicit numerical stencil can be constructed for a temporal layer  $\delta\tau$  in a form

$$\hat{U}_{j,l}^{n+1} = \hat{U}_{j,l}^n + \hat{U}'_{j,l} + \hat{U}''_{j,l} - \lambda_1 \hat{E}_{j,l} - \lambda_2 \hat{F}_{j,l} + \delta\tau \hat{S}_{j,l}^n, \quad (14)$$

where  $\hat{U}_{j,l} = (\hat{U}_{j,l,k})$ ,  $k = 1, 2, 3$ ,  $\lambda_1 := \delta\tau/\delta\xi$ ,  $\lambda_2 := \delta\tau/\delta\eta$ ,  $\tau^n = n\delta\tau$ , and the prime and double-prime notations represent the discrete derivatives in the  $\xi$ -direction and  $\eta$ -direction, respectively.

In the present simulation, a third-order accurate scheme proposed by Jiang *et al.*<sup>53</sup> is used with a “minmod”-limiter. If denote  $w$  as a variable, a “minmod” limiter can be given as

$$w'_j = \min\left(\Delta w_{j+1/2}, \frac{1}{2}(w_{j+1} - w_{j-1}), \Delta w_{j-1/2}\right), \quad (15)$$

where  $\Delta w_{j-1/2} \equiv w_j - w_{j-1}$ ,  $\Delta w_{j+1/2} \equiv w_{j+1} - w_j$ .

The CFL condition is determined by the maximum wave speed  $a^{\max}$  as follows<sup>46</sup>

$$a^{\max} \frac{\delta\tau}{\max(\delta\xi, \delta\eta)} < 1, \quad \forall j, l, \quad (16)$$

with

$$a^{\max} = \max\left(\hat{u} \pm c(\xi_x^2 + \xi_y^2)^{1/2}, \hat{v} \pm c(\eta_x^2 + \eta_y^2)^{1/2}\right), \quad (17)$$

where  $c = \sqrt{h \cos \zeta}$ , and  $\hat{u}$  and  $\hat{v}$  are obtained according to Eq. (13).

### III. SET-UP FOR THE LABORATORY EXPERIMENT AND COMPUTER SIMULATION

#### A. The set-up and measurement in the experiment

In order to operate practically in the experiment, a two-gate system is established within the 15 by 10 test area, as shown in Fig. 3, to control the start of the granular flow at the inlet and the formation of the strong oblique shock wave from the outlet, respectively. To further illustrate the settings, a schematic of the experiment set-up is shown in Fig. 4. The experiment was carried out on a plexiglass chute that was 40 units (or 1200 mm) long and 10 units (or 300 mm) wide, inclined at an angle  $\zeta = 38^\circ$  to the horizontal. A hopper was placed at the top of the chute, where the granular material, 100's and 1000's sprinkles with a diameter of 1mm, can be stored and then released through a gate, i.e the first gate or upstream gate. This gate controls the inlet conditions of the flow and is aligned at  $x = 0$ , where the inlet boundary conditions are defined by the initial flow thickness  $h_0$  and initial downslope velocity  $\bar{u}_0$  since the cross-slope velocity  $\bar{v}_0 = 0$ . To obtain these values, the flow velocity was measured with a particle image velocimetry (PIV) device and the flow thickness was measured along the transparent sidewall with a micrometer, giving  $h_0 = 0.72$  (or 22 mm) and  $\bar{u}_0 = 1.013$  (or 0.55 m/s), which implies a supercritical flow from the inlet as the Froude number  $Fr_0 = 1.34$ .

Whether the flow propagating further down the slope is accelerative or not depends on the difference between the inclination angle  $\zeta$  and the basal friction angle  $\delta$ . Simplifying the downslope source term of (4) for one-dimensional and straight chute surface conditions leads to

$$S^x = \sin \zeta - \tan \delta \cos \zeta = \frac{\sin(\zeta - \delta)}{\cos \delta}. \quad (18)$$

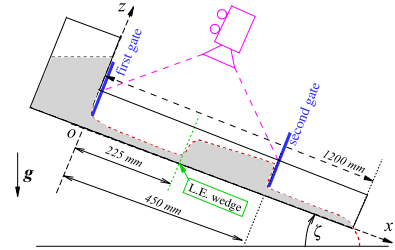


FIG. 4: A schematic of the experiment set-up for the granular free-surface flow down a chute, where the leading edge (L.E.) of the wedge is denoted for its location.

Therefore, non-accelerative flows can occur as well if  $\zeta \leq \delta$ , but the present work will focus on the accelerative flow only. To obtain a realistic value of  $\delta$ , the PIV device was used to measure the velocity distribution of the test area by starting the same flow from the first gate, but making it move down the chute without encountering any obstacle. By matching this measured velocity distribution with the numerical solution of  $\bar{u}$  for the one-dimensional flow under the same  $h_0$ ,  $\bar{u}_0$  and  $\zeta$ , a value of  $\delta = 23^\circ$  was obtained<sup>36</sup>. Therefore, the flow here is fully accelerative along the chute since  $\zeta$  is much greater than  $\delta$ .

Away from the first gate, an oblique wedge was now placed at a downslope position  $x = 7.5$ . This wedge was 8 units long and was deflected at an angle  $\theta = 20^\circ$  against the sidewall of the chute. Placed immediately downstream of this wedge was the second gate (or downstream gate), of which height,  $h_{1,\text{exp}}$ , and opening time,  $t_{1,\text{exp}}$ , were controlled such that the strong oblique shock wave could form from the leading edge of the wedge.

To better understand  $h_{1,\text{exp}}$  and  $t_{1,\text{exp}}$ , let us briefly explain the formation process of a strong oblique shock wave. When a granular material is released from the first gate at the top of a chute, a weak oblique shock wave first appears along the wedge as the flow is deflected by it. As the flow propagates further downstream and is blocked by the second gate, a normal shock wave forms there and travels back upstream as a strong shock wave. At the instant when the strong shock wave moves upstream to near the leading edge, i.e. at  $t = t_{1,\text{exp}}$ , the second gate is opened, allowing the blocked material to flow out downstream at a controlled height of  $h_{1,\text{exp}}$ . As time progresses further, this strong shock wave gradually steadies as a strong oblique shock wave by attaching to the leading edge of the wedge.

In order to determine the actual values of  $h_{1,\text{exp}}$  and  $t_{1,\text{exp}}$ , a few trial tests were conducted in the experiment to ensure the generation of the strong oblique shock wave, where each test was an attempt for a set of combined values of  $h_{1,\text{exp}}$  and  $t_{1,\text{exp}}$ . In the present case,  $h_{1,\text{exp}}$  is shown to be  $20 \pm 1$  mm (or  $0.6667 \pm 0.0333$ ), and  $t_{1,\text{exp}} =$

$1.60 \pm 0.04$  seconds (or  $28.9 \pm 0.72$ ). This is an interesting result because  $h_{1,\text{exp}}$  here is very close to the inlet flow thickness,  $h_0 = 22$  mm (or 0.72). Since this wedge has a length  $l_w = 8$  and is deflected by  $\theta = 20^\circ$ , the second gate thus has a lateral width  $W_1 = 7.26$ . With the first gate having a width  $W_0 = 10$ , one may say that the heights of the first gate and the second gate can be kept approximately equivalent if their lateral widths are wide enough.

#### B. The set-up and implementation in the computer simulation

As shown in Fig. 3, the set-up of the computational domain has been kept identical to the test area designed for the above experiment. To follow the flow propagation naturally, an H-type grid, with a size of  $196 \times 201$  gridpoints, is used in the simulation to cover a domain of  $0 \leq x \leq 15$  and  $0 \leq y \leq 10$ , respectively. This grid size has been checked through the preliminary test and is sufficient to ensure an accuracy of simulation with a residual of below  $10^{-6}$ , e.g., in Fig. 5. The inlet conditions,  $h_0 = 0.72$ ,  $\bar{u}_0 = 1.013$  and  $\bar{v}_0 = 0$ , are given at  $x = 0$  for the left boundary. For the outlet conditions on the right boundary, they will be given in a similar manner as in the experiment to mirror the settings for the second gate.

Although the inlet flow has one-dimensional features, the outlet flow at the downstream of the wedge is two-dimensional since both  $h_1$  and  $\bar{\mathbf{u}}_1 = (\bar{u}_1, \bar{v}_1)$  can vary over  $W_1$ . To provide an effective and direct outflow flux for the outlet condition, one introduces an average mass flux that is only based on the downslope component  $\bar{u}_1$

$$\bar{m}_1 = \frac{1}{W_1} \int_0^{W_1} h_1 \bar{u}_1 dy. \quad (19)$$

Let  $t_{1,\text{compt}}$  be the opening time for the outlet condition, then  $\bar{m}_1$  can be controlled as follows

$$\bar{m}_1 = \begin{cases} 0 & t < t_{1,\text{compt}}, \\ \bar{m}_{1,\text{compt}} & t \geq t_{1,\text{compt}}, \end{cases} \quad (20)$$

where  $\bar{m}_{1,\text{compt}}$  is the actual value used in the simulation. Similarly, the determination of  $\bar{m}_{1,\text{compt}}$  and  $t_{1,\text{compt}}$  can be done through a few trial simulations. According to equation (8), a good initial guess of  $\bar{m}_{1,\text{compt}}$  can be obtained by letting it be  $h_0 \bar{u}_0 W_0 / W_1$ .

For the current example, since  $W_0 = 10$  and  $W_1 = 7.26$ , one can have an initial value,  $\bar{m}_{1,\text{compt}} = 1.005$ . Fig. 5 shows the time evolutions of the average flow thickness,  $h_{\text{ave}}$ , and its residual,  $\delta h$ , for  $\bar{m}_{1,\text{compt}} = 1.005$ , 0.995 and 0.97, respectively, under a fixed  $t_{1,\text{compt}} = 27.0$  (i.e., 1.49 seconds). Here,  $h_{\text{ave}}$  and  $\delta h$  are calculated by

$$h_{\text{ave}}^{(n)} = \frac{\sum_{i=1}^{N_x} \sum_{j=1}^{N_y} h_{i,j}^{(n)}}{N_x N_y}, \quad \delta h^{(n)} = |h_{\text{ave}}^{(n)} - h_{\text{ave}}^{(n-1)}|, \quad (21)$$

where  $N_x$  and  $N_y$  represents the numbers of the grid-points in the  $x$ - and  $y$ -directions, respectively, and the superscript  $(n)$  represents the progress of simulation in the time domain. It is seen that a steady-state solution has achieved when  $\bar{m}_{1,\text{compt}} = 0.995$ , while the initial guess of  $\bar{m}_{1,\text{compt}} = 1.005$  appears to be slightly “under blocking” the outlet boundary, but such fluctuation is only within an error of 1%. The result for the opening time  $t_{1,\text{compt}}$  agrees broadly well with the experiment,  $t_{1,\text{exp}} = 28.9 \pm 0.72$  (or  $1.60 \pm 0.04$  seconds), having an error of 7%.

#### IV. FORMATION OF THE STRONG OBLIQUE SHOCK WAVE

Following the set-up of the above two-gate system, the inlet conditions for the first gate are given by  $h_0 = 0.72$ ,  $\bar{u}_0 = 1.013$  and  $\bar{v}_0 = 0$  under  $\zeta = 38^\circ$  and  $\delta = 23^\circ$ , identical between the experiment and the simulation. For the outlet conditions at the second gate, the experiment settings are  $h_{1,\text{exp}} = 20 \pm 1$  mm and  $t_{1,\text{exp}} = 1.60 \pm 0.04$  seconds, and the simulation settings are  $\bar{m}_{1,\text{compt}} = 0.995$  and  $t_{1,\text{compt}} = 1.49$  seconds.

Since the granular flowing process around the wedge was recorded by a video camera, the time interval between two consecutive frames is equal to 0.08 seconds. As shown in Fig. 6, in order to focus on recording the primary flow region, the horizontal length of the camera's window was limited to a range of  $5.4 \leq x \leq 15$ , while the lateral width can be kept at  $0 \leq y \leq 10$ . This means that only when the front of the granular flow entered the window could the first “meaningful” or blank-free image be captured and then used for comparison, as shown in Fig. 6a. In fact, this corresponds to a time-dependent solution at 0.12 seconds, or 2.17 units of dimensionless time, in the simulation.

In order to observe and compare the formation process of the strong oblique shock wave in the experiment and simulation, a series of time-evolving sequences are shown in figures 6 and 7, where the images denoted by “(a)” to “(l)” are long-exposure snapshots of the flow taken in the experiment, and the corresponding flow thickness contours obtained in the simulation are labelled for the time nodes from 0.12 to 2.84 seconds.

For the first three consecutive sequences in Fig. 6, namely, images (a-c) and the flow thickness contours corresponding to  $t = 0.12$ , 0.20 and 0.28 seconds, the front of the flow moves rapidly from left to right along the chute. As the flow only has a thin layer at the front at these instants, it is difficult to observe any form of shock wave from the experiment. However, as shown in the solution of 0.20 seconds, once the front of the flow has hit the tip of the wedge, even a very weak form of shock can be captured in the numerical simulation. In fact, the solution of 0.28 seconds suggests that this weak shock wave travels downstream slightly faster than the moving front of the flow.

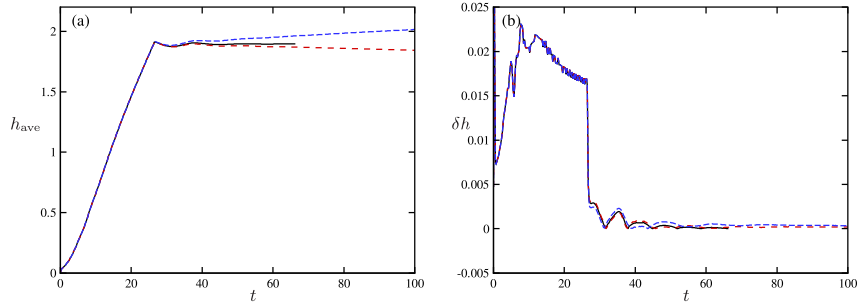


FIG. 5: Evolution history of (a) the average flow thickness  $h_{ave}$ , (b) the residual of  $h_{ave}$ . Three outflow fluxes,  $\bar{m}_1 = 1.005, 0.995$  and  $0.97$  have been tested under the same  $t_{1,compt} = 27$ , where in each of the graphs, the dashed line is for  $\bar{m}_1 = 1.005$  which represents an initial guess for  $\bar{m}_1$  according to (19), the dashdot line is for  $\bar{m}_1 = 0.97$ , and the solid line is for  $\bar{m}_1 = 0.995$  where a steady-state solution has achieved for  $\delta h \leq 10^{-6}$ .

The numerical solution at 0.60 seconds and its experimental image (d) start to show a more complex structure. Since the second gate, which is aligned with the right boundary, remains blocked until the opening time is reached, a strong shock wave is first formed there and propagates back upstream. In this early stage of upstream propagation, this strong shock region is characterized by two forms of shock – a bow shock wave that interacts with the weak oblique shock wave near the wedge, and a normal shock that connects the bow shock and extends to the sidewall at the far end. This part of normal shock wave still has features of one-dimensional flow, or one can say, if the granular flow is only blocked by the downstream gate in an obstacle-free chute, then the back-propagating wave will only be a simple normal shock<sup>4</sup>.

As this strong shock region travels further upstream, the normal shock merges quickly with the bow shock, forming a single strong shock wave. From images (e-f) in Fig. 6 and all the images in Fig. 7, as well their corresponding time-specified numerical solutions in these figures, one can see that this strong shock wave develops continuously with time, while moving to the upstream and interacting with the weak oblique shock wave, and settles as a steady-state solution, as shown by the 2.84 second solution and image (l) in Fig. 7. The results for the 1.48 seconds and 1.64 seconds are of particular interest as the solution of 1.48 seconds corresponds to the second gate opening time,  $t_{1,compt} = 1.49$  seconds, used in the simulation, where the position of the strong shock wave is around  $x = 10$ . For the solution of 1.64 seconds, the strong shock wave moves to a position of  $x = 8.6$ , much closer to the leading edge of the wedge, but this instant is around the opening time of the second gate used in the experiment because  $t_{1,exp} = 1.60 \pm 0.04$  seconds. Also observed in these time-evolving solutions is the appearance of a “thickness concentration” zone towards the trailing edge of the wedge, in which the thickness  $h$  increases even more significantly. Such features can also be seen in images (g-i), where, in similar areas

near the wedge, the camera’s long-exposure does not blur the static state of the particles, so the details are clearly visible. In the last three numerical solutions of Fig. 7, it can be seen that both the shape and the attachment point of the strong oblique shock wave still undergo further adjustment when approaching the steady state of 2.84 seconds.

## V. INTERACTIONS BETWEEN WEAK AND STRONG SHOCK WAVES

### A. Time-dependent interaction between the weak oblique and bow shocks

During the formation of the strong oblique shock wave, there are continuous time-dependent interactions between the weak and the strong shocks once the granular flow reaches the second gate, persisting until the weak oblique shock disappears at the tip of the wedge. Following the definition of the shock-shock interactions for gasdynamic problems by Edney (1968)<sup>54</sup>, Grasso<sup>55</sup> summarized the interaction characters in a simpler manner, whereas the interaction between weak and strong shocks can be referred as a type III or type IV interaction.

To give a clearer picture about the early stage details of the flow impacting the second gate of downstream, further transient solutions of flow thickness  $h$ , based on the same simulation conducted for Fig. 6, are shown in Fig. 8. In these time sequences, the 0.30 second solution shows an instant of the flow just prior to the impact, where the oblique shock propagates to the downstream faster than the rest of the flow. At the time of 0.31 seconds, the front of the oblique shock reaches the second gate first, and a shock interaction starts to appear near the trailing edge of the wedge (also, see an inset in this plot). Shortly at 0.33 seconds, the normal shock and its interaction with the oblique shock become clearer, and are continuously strengthened, while moving back



This is the author's peer reviewed, accepted manuscript. However, the online version of record will be different from this version once it has been copyedited and typeset.

PLEASE CITE THIS ARTICLE AS DOI: 10.1063/5.0057700

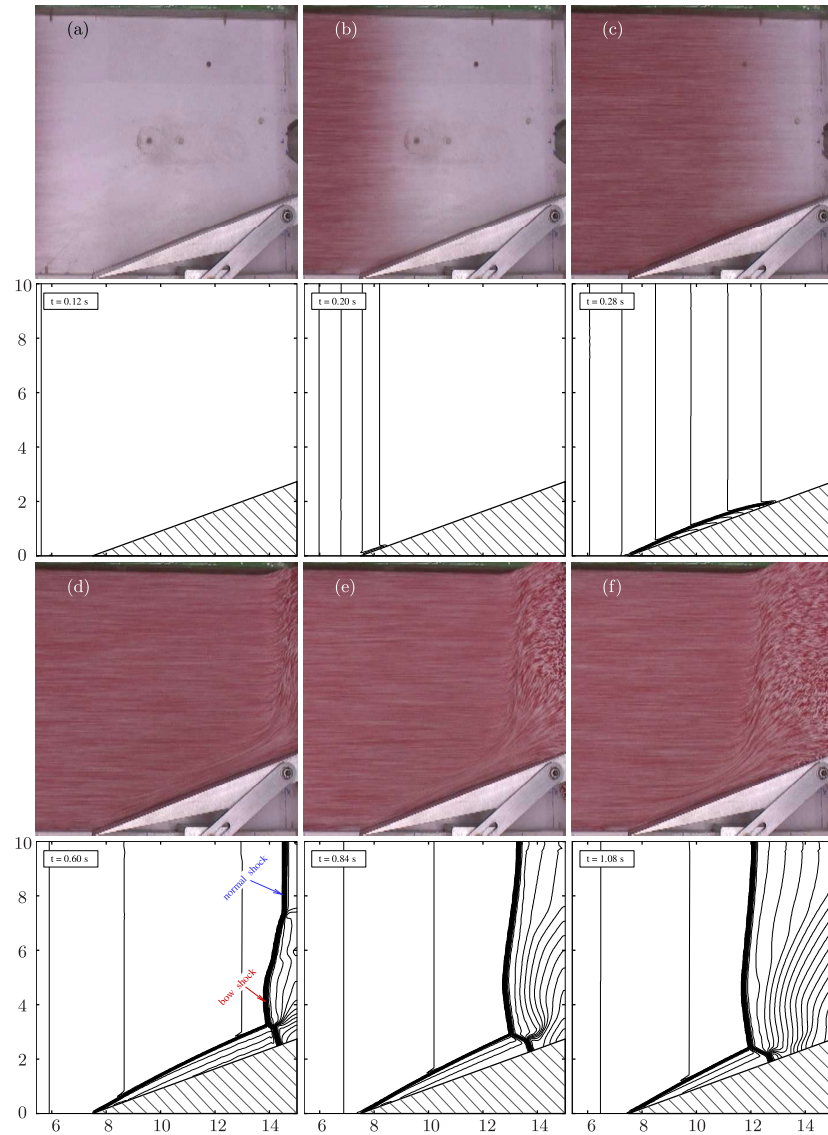


FIG. 6: Experimental images and computational solutions of  $h$  for a granular avalanche propagating against a wedge of angle  $\theta = 20^\circ$ . The experimental images are long-exposure “snap-shots”, labelled from (a) to (f), corresponding to the computational solutions of  $h$  at  $t = 0.12, 0.20, 0.28, 0.60, 0.84, 1.08$  seconds, respectively. The flow orientation is from left to right in each of the panels.

upstream, in the solutions for 0.37, 0.39 and 0.44 seconds. An inset of the color map of  $h$  is added to the 0.37



This is the author's peer reviewed, accepted manuscript. However, the online version of record will be different from this version once it has been copyedited and typeset.

PLEASE CITE THIS ARTICLE AS DOI: 10.1063/5.0057700

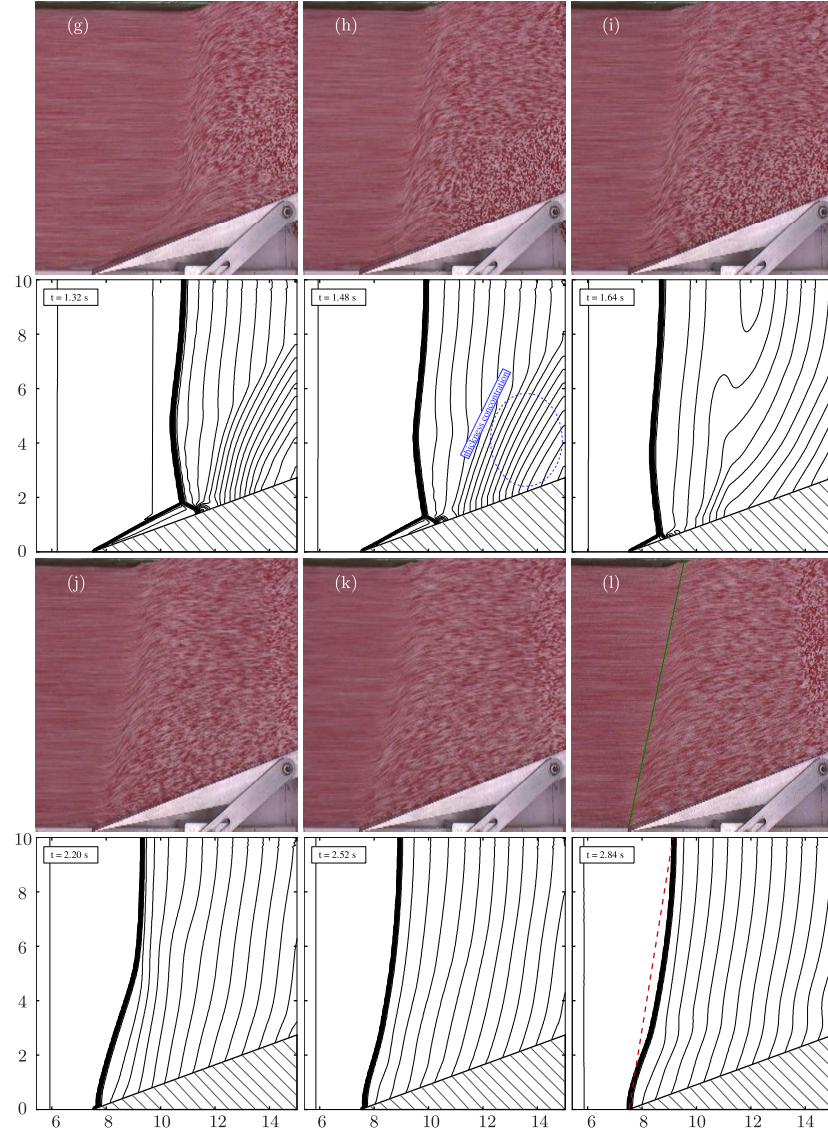


FIG. 7: Further time-dependent results on the formation of the strong oblique shock wave, where the experimental images are labelled from (g) to (l) continuously from Fig. 6, corresponding to the computational solutions of  $h$  at  $t = 1.32, 1.48, 1.64, 2.20, 2.52, 2.84$  seconds, respectively. A shock angle of  $78^\circ$  is achieved for the steady-state oblique shock in image (l) and  $t = 2.84$  second plot, highlighted in green solid line and red dash line, respectively.

second plot, where a bow shock starts to take its shape around this instant. Thus, one can refer such shock inter-

action, taking place between oblique (or incident) shock and bow shock, to a type IV structure<sup>54,55</sup>, but there are clear differences between gasdynamic and granular flows. Among these, the change of the flow speed, represented by the Froude number or the Mach number, in the region downstream of the oblique shock differs significantly. As shown in Fig. 9, for the times of 0.46 to 1.48 seconds, the Froude number of the flow is totally subcritical ( $Fr < 1$ ) in the downstream of the oblique shock, whereas in gasdynamics the Mach number of the flow in a similar region remains supersonic (i.e. above 1). Another difference between granular flow and gasdynamic flow is the interpretation of the so-called “slip line”. On this slip, as long as the pressures are balanced, the flow velocities from two adjacent layers along this line can slip, but this has not been, or at least not clearly, observed in the simulation here.

Besides, a supercritical region,  $Fr > 1$ , is observed in the 1.60 second solution of Fig. 9, and this feature will be clearer when the shock interaction becomes a steady-state solution.

#### B. Steady-state interaction between the weak and strong oblique shocks

During the experiment it was also observed that, if the second gate's height  $h_{1,\text{exp}}$  was kept fixed, say, around  $20 \pm 1$  millimeters, different forms of shock wave could be achieved as steady state by only changing  $t_{1,\text{exp}}$ . For example, if  $t_{1,\text{exp}}$  was set greater than  $1.60 \pm 0.04$  seconds, a strong normal shock would appear somewhere upstream the wedge<sup>4</sup>. If  $t_{1,\text{exp}}$  was set smaller, an interaction of weak and strong oblique shocks would appear as steady state somewhere in-between the wedge, as shown in Fig. 10. In this figure, a different opening time,  $t_{1,\text{exp}} = 0.92 \pm 0.04$  seconds, was used for opening the second gate in the experiment, while other conditions including the height of the second gate remain unchanged. Also shown in Fig. 10 are the steady-state solutions of the flow thickness and Froude number obtained in the simulation, where a numerical opening time,  $t_{1,\text{compt}} = 0.84$  seconds, is used, and this gives an error of 8.7% with the comparison to the experimental time of 0.92 seconds. In addition, the outflow flux  $\bar{m}_{1,\text{compt}}$  used in the simulation was only adjusted to 0.992.

Further comparing the shape of the steady shock interaction with that of the transient's, e.g., of 1.08 seconds in Fig. 6 or of 1.32 seconds in Fig. 7, one can see that the branch of the strong shock here becomes more oblique since the flow upstream the shock has fully developed as an accelerative steady flow along the slope under a  $38^\circ$  inclination over a basal friction angle of  $23^\circ$ . Another interesting change of the flow behaviours is that the flow field downstream the weak oblique shock remains largely supercritical, and this feature is even closer to its gasdynamics counterpart.

The comparison between the time-dependent interac-

tion and the steady-state interaction of shocks suggests that there may exist close relations between these two types of interaction, not just for the shape of it, but maybe more practically, for the determination of the numerical opening time  $t_{1,\text{compt}}$ . To do this, one further tracked the move of the position of the shock intersection, e.g. point  $x_s$  annotated in the 0.44 second plot of Fig. 8, in the time-dependent simulation of the strong oblique shock. As shown in Fig. 11a, the position of the shock intersection point  $x_s$ , in non-dimensional units and marked by symbol  $\Delta$ , moves approximately linearly with the increase of time (in seconds). To give a better comparison, a linear best fit is provided, where a relation  $x_s = -4.73t + 16.29$  is obtained, and is shown in solid line alongside the  $\Delta$  markers. For this linear trend line, since the gradient coefficient 4.73 has a unit of seconds<sup>-1</sup>, one can re-scale it to  $u_s = 0.1419$  m/s (or 0.2617 units), as a moving rate for the intersection point  $x_s$ .

Using this rate, one can approximate the time used for a shock intersection point to move from the leading edge of  $x_s = 7.5$  to a designated location, say,  $x_s = 10.8$  required for the present steady-state intersection in Fig. 10. This then yields a time gap of 12.61 units (or 0.6793 seconds, and for simplicity the use of dimensional unit is dropped thereafter). That is to say, if the opening time required for generating a strong oblique shock of steady-state is known, e.g.  $t_{1,\text{compt}} = 27.0$ , then the opening time for achieving a steady-state interaction between weak and strong oblique shocks, for example, at  $x_s = 10.8$ , can be approximated by  $t_{1s,\text{appx.}} = 27.0 - 12.61 = 14.39$ . This gives an error of 5.6% with the comparison to the actual opening time,  $t_{1s,\text{compt}} = 15.24$ , used for Fig. 10's simulation.

The rate of change,  $dx_s/dt$ , of the above individual markers in Fig. 11a is further studied by applying the trapezium rule to the  $\Delta x_s/\Delta t$  operations. This moving rate is denoted by  $u_{si}$  (in m/s) and marked with circular points in Fig. 11b. It can be seen from these results that the shock intersection does not move upstream at a constant rate, but approaches the tip of the wedge with a tendency of gradually becoming smaller. A few trend lines are provided along these markers in this figure, where the solid line represents a quadratic trend  $u_{si} = 0.0475t^2 - 0.1341t + 0.2291$ , the dashdot line represents a linear trend  $u_{si} = -0.0296t + 0.1855$ , and the dashed line is an average of the marker's values over time so  $u_{s,\text{ave}} = 0.1516$  m/s (or 0.2796 units). Repeating a similar calculation as above, this average value of  $u_{s,\text{ave}}$  then gives an estimate of the numerical opening time  $t_{1s,\text{ave}} = 15.20$  units (or 0.841 seconds). This is a surprisingly close, nearly identical result since the actual opening time used in the simulation is 15.24 units. One reason may be that, since this shock intersection takes place at a mid-wedge location  $x_s = 10.8$ , its actual moving rate is closer to  $u_{s,\text{ave}}$ . Therefore, using the moving rate of the shock intersection can provide a more measurable estimation for the second gate's opening time, which would make simulation and experiment more easily op-

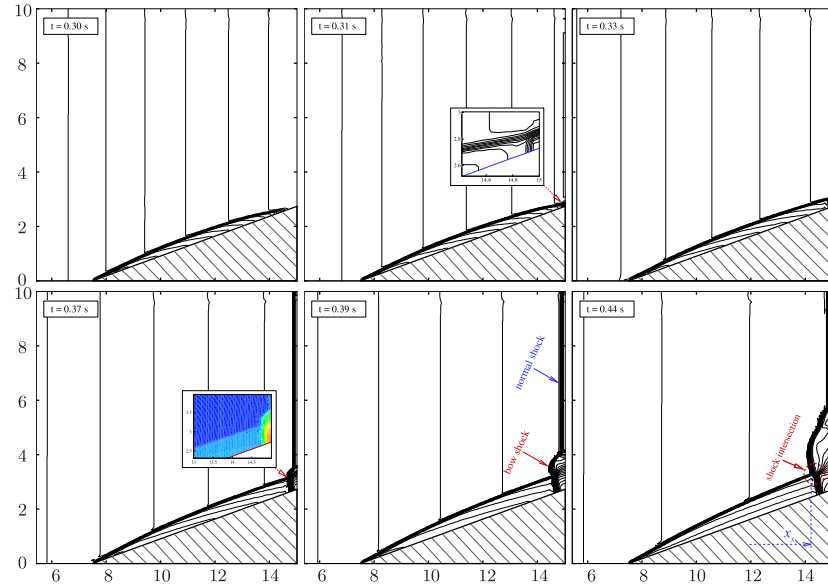


FIG. 8: Time-dependent numerical solutions of flow thickness  $h$  for  $t = 0.30, 0.31, 0.33, 0.37, 0.39$  and  $0.44$  seconds, showing the early stage of the back-to-upstream propagation of strong shocks, when the flow is blocked by the second gate of downstream. As the weak oblique shock arrives the gate first around  $0.31$  seconds, a bow shock appears by interacting with the oblique shock near the wedge. Away from this near-wedge region, a one-dimensional normal shock is generated and travels back stream. The conditions here are the same as used in figures 6 and 7.

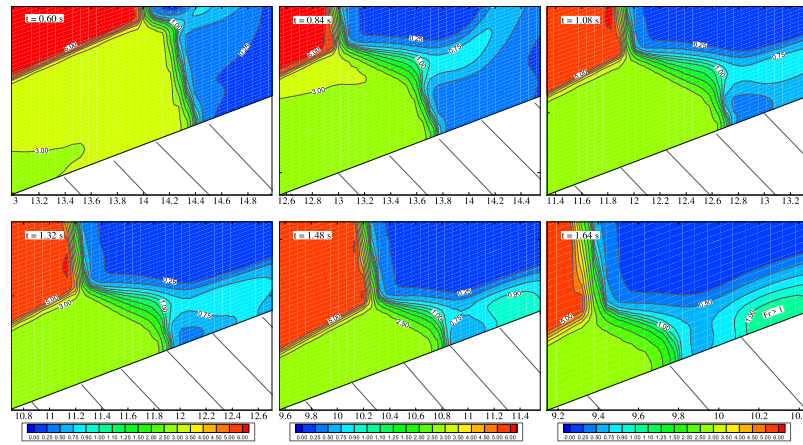


FIG. 9: Time-dependent contours of Froude number near the shock interaction region, obtained at times of  $0.60, 0.84, 1.08, 1.32, 1.48$  and  $1.64$  seconds that correspond to the numerical solutions in figures 6 and 7.

erated, if the location of the shock intersection point is known in advance.

### C. A numerical test on the effect of the basal friction

Since the basal friction,  $\mu = \tan \delta$ , is an important factor affecting the flow behaviour through the source

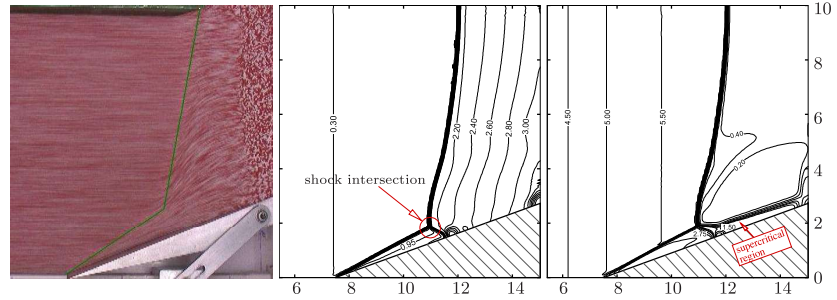


FIG. 10: Steady-state interaction of weak and strong oblique shock waves, where the left-panel is a long-exposure photo taken from the experiment, the middle- and right-panels are flow thickness  $h$  and Froude number  $Fr$ , respectively, obtained in the numerical simulation. A green line is added to the experimental result to show the fronts of the weak and strong shocks.

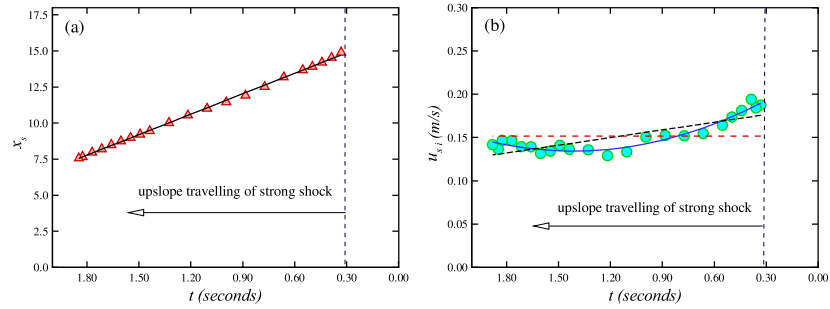


FIG. 11: The upslope travelling of the intersected shock with time, obtained from the transient numerical solutions. Panel (a) shows variation of the position of the shock intersection point,  $x_s$  (in non-dimensional units here), with time (in seconds), where the markers of  $\Delta$  denote the numerical solutions, and the solid line is obtained by a linear best fit so that  $x_s = -4.73t + 16.29$ . Panel (b) shows variation of the travelling rate of point  $x_s$  along the upslope direction, denoted by  $u_{s,i}$  (in m/s), with time, where the circular markers represent the numerical results, and the solid line, dashdot line and dashed line represent the trend lines of quadratic, linear and average, respectively. Note that the direction of the horizontal axis  $t$  here has been reversed.

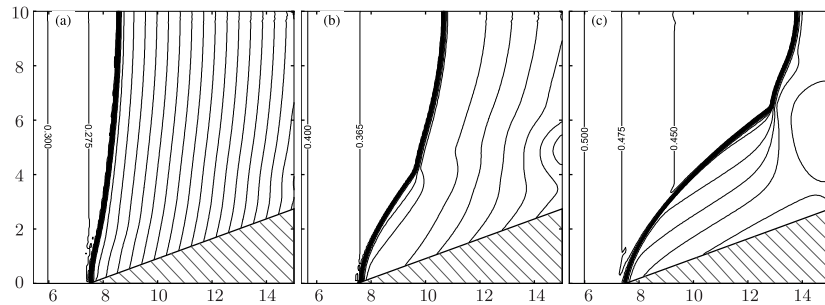


FIG. 12: The steady-state solutions of  $h$  for the strong oblique shock with different basal friction angles, where (a)  $\delta = 18^\circ$ , (b)  $\delta = 30^\circ$ , and (c)  $\delta = 35^\circ$ .

terms given in (4), a further numerical test has been conducted by varying the basal friction angle  $\delta$  while keep-

ing other conditions unchanged. To obtain such solutions in the simulation, the inlet conditions for the first gate



and the outlet conditions for the second gate remain exactly the same as used in Section IV, namely,  $h_0 = 0.72$ ,  $\bar{u}_0 = 1.013$ ,  $v_0 = 0$ ,  $\bar{m}_{1,\text{compt}} = 0.995$  and  $\zeta = 38^\circ$ , and the only change is the use of different opening time of the second gate  $t_{1,\text{compt}}$ . As shown in Fig. 12, three angles of  $\delta$ ,  $18^\circ$ ,  $30^\circ$  and  $35^\circ$ , are used in the simulation. Corresponding to these solutions are the different values of  $t_{1,\text{compt}}$ , where (a)  $t_{1,\text{compt}} = 29.1$ , (b)  $t_{1,\text{compt}} = 19.75$ , and (c)  $t_{1,\text{compt}} = 13.3$ . With the increase of  $\delta$ , and thus of  $\mu$ , one can see in the figure that the strong oblique shock becomes more oblique towards the downstream. This is because the incoming Froude number at the front of the wedge becomes smaller with the increase of  $\delta$ , e.g., (a)  $\text{Fr}_1 = 5.75$ , (b)  $3.73$  and (c)  $2.52$ , thus the corresponding shock angle  $\beta$  becomes smaller too (see, Fig. 1). Another interesting observation is that, these numerical solutions can be obtained by only changing  $t_{1,\text{compt}}$  while the outflow flux  $\bar{m}_{1,\text{compt}}$  remains exactly the same as used previously. With the increase of  $\delta$ , the gravitational effect that accelerates the flow to downstream becomes smaller, as suggested in (18). It then allows the strong shock to travel back upstream at a faster rate after being stopped by the downstream gate, hence  $t_{1,\text{compt}}$  gets smaller as a result.

## VI. CHANGE OF THE INERTIAL NUMBER ACROSS SHOCK WAVES

### A. The bulk inertial number of granular free-surface flows

With reference to the inertial number,  $I$ , defined in equation (1), Holyoake & McElwaine (2012)<sup>18</sup> used a bulk inertial number, denoted  $I_b$ , to express the bulk effect for granular free-surface flow. In particular they re-defined the local shear rate in a form

$$\dot{\gamma}_w = \frac{|\tilde{\mathbf{u}}_b|}{\tilde{h}}, \quad (22)$$

where  $\tilde{h}$  is the dimensional flow thickness, and  $\tilde{\mathbf{u}}_b$  refers to the velocity at free surface, but is assumed to be the same as the depth-averaged velocity. Similarly, the tilde notation here is used to denote a dimensional term.

For the normal hydrostatic pressure  $P$  used in (1), one defines it as follows. Let  $P_z$  be the pressure distribution normal to the chute basal surface, i.e. along the positive  $z$ -axis by pointing upward, and it can be given as

$$P_z = \rho g(\tilde{h} - z) \cos \zeta \quad (23)$$

over a normal height of  $\tilde{h}$ . Integrating  $P_z$  over  $\tilde{h}$  and depth-averaging the product then yields a depth-averaged hydrostatic pressure

$$\bar{P} = \frac{1}{\tilde{h}} \int_0^{\tilde{h}} P_z dz = \frac{1}{2} \rho g \tilde{h} \cos \zeta. \quad (24)$$

Since  $\sqrt{g\tilde{h} \cos \zeta}$  is the dimensional sound speed of wave propagation, one can have another form for the Froude number

$$\text{Fr} = \frac{|\tilde{\mathbf{u}}_b|}{\sqrt{g\tilde{h} \cos \zeta}}. \quad (25)$$

Substituting (22), (24) and (25) into (1) gives

$$I_b = \sqrt{2} \frac{\tilde{d}}{\tilde{h}} \text{Fr} \quad \text{or} \quad \sqrt{2} \frac{d}{h} \text{Fr}, \quad (26)$$

which can be directly applied to granular free-surface flows. For the granular flow studied in this paper, since  $\text{Fr} = 5$  at the front of the wedge, and with  $h = 0.3$  and  $d = 1/30$ , one can have a bulk inertial number,  $I_{b1} = 0.7071$ , upstream the shock wave.

### B. The ratio of the bulk inertial number across shock waves

To follow the change of the inertial number,  $I_b$ , across shock waves, a ratio of  $I_b$ , denoted  $I_r$ , is introduced in the following form

$$I_r = \frac{I_{b2}}{I_{b1}}, \quad (27)$$

where the subscripts “1” and “2” represents the flow conditions upstream and downstream of shock wave, respectively. Therefore, substituting (26) into (27) gives

$$I_r = \frac{\tilde{h}_1 \text{Fr}_2}{\tilde{h}_2 \text{Fr}_1} \quad \text{or} \quad \frac{h_1 \text{Fr}_2}{h_2 \text{Fr}_1} \quad (28)$$

since the grain diameter  $\tilde{d}$  is unchanged. Further relating (28) directly with the change in flow velocity and thickness across shock gives

$$I_r = \frac{|\tilde{\mathbf{u}}_2|}{|\tilde{\mathbf{u}}_1|} \left( \frac{h_1}{h_2} \right)^{3/2}. \quad (29)$$

With the following oblique shock relations<sup>33</sup>

$$\begin{aligned} \frac{|\tilde{\mathbf{u}}_2|}{|\tilde{\mathbf{u}}_1|} &= \frac{\cos \beta}{\cos(\beta - \theta)} \\ \frac{h_2}{h_1} &= \frac{\tan \beta}{\tan(\beta - \theta)}, \end{aligned} \quad (30)$$

one can have

$$I_r = \frac{\cos \beta}{\cos(\beta - \theta)} \left( \frac{\tan(\beta - \theta)}{\tan \beta} \right)^{3/2}, \quad (31)$$

which directly relates the change of the bulk inertial number across shock wave with the shock angle  $\beta$  and the wedge angle  $\theta$ .



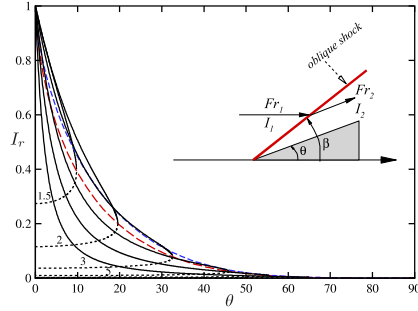


FIG. 13: Ratio of the inertia number  $I_r = I_{b2}/I_{b1}$  across shock wave, as a function of the wedge angle  $\theta$  for  $Fr_1 = 1.5, 2, 3, 5, 8, 15$ . The solid lines correspond to the weak shock, the short-dashed lines correspond to the strong shock, the long-dashed line marks the transition  $\theta_{\max}$ , and the dotted line marks the  $Fr_2 = 1$ .

A theoretical solution of  $I_r$  can be obtained with the use of the oblique shock relation (5), as shown in Fig. 13. It is seen that the change of  $I_r$  across a strong oblique shock is far greater than that across a weak oblique shock. For example, for  $Fr = 5$  and  $\theta = 20^\circ$ ,  $I_r$  is equal to 0.157 across a weak shock, but only  $9.85 \times 10^{-3}$  across a strong shock. Or if the inertial number upstream the shock is  $I_{b1} = 0.7071$ , it then reduces to an inertial number of 0.111 at the downstream of the weak oblique shock, but at the downstream of the strong oblique shock the corresponding inertial number is only equal to  $6.96 \times 10^{-3}$ , for the case studied in this paper.

## VII. CONCLUSIONS

The formulation of the oblique shock relation of granular flow (Gray & Cui 2007<sup>33</sup>) suggests that there exists a strong oblique shock wave for a given incoming Froude number,  $Fr_1 > 1$ , if the flow is deflected by a wedge angle  $\theta$  that is smaller than the detachment angle  $\theta_{\max}$ . To generate such a strong oblique shock solution in experiment, the channelized granular flow on an inclined chute needs to be enclosed by a two-gate system, in which the first gate provides the inlet conditions at the top of the chute, and the second gate, of which height  $h_{1,\text{exp}}$  and opening time  $t_{1,\text{exp}}$  need to be controlled, provides the right outlet conditions at the downstream of the wedge. In the simulation of such two-dimensional chute flow, correspondingly, the left boundary of the computational domain should act as the first gate, providing the inlet conditions for  $h_0$  and  $\bar{u}_0$ , whereas the right boundary should act as the second gate, which is controlled by the outlet conditions defined by the outflow flux  $\bar{m}_{1,\text{compt}}$  and the numerical opening time  $t_{1,\text{compt}}$ . As the flow is driven by the gravitational force but resisted by the basal friction,

the example studied in this paper is fully accelerative for  $\zeta = 38^\circ$  and  $\delta = 23^\circ$ , and hence the Froude number of the flow can be accelerated from  $Fr_0 = 1.34$  at  $x = 0$  to  $Fr_1 = 5$  at  $x = 7.5$ . With such an incoming Froude number at the upstream of the wedge, the strong oblique shock wave is predicted to appear at an angle of  $86.15^\circ$ , but both the experiment and simulation suggest that it has an actual angle around  $78^\circ$  due to the effect of the flow acceleration (Fig. 7).

During the time-dependent evolution of the strong oblique shock wave, there undergo instantaneous interactions between the weak and strong shock waves. This is because the weak oblique shock wave always first appears once the flow impacts the leading edge of the wedge while the strong shock wave only starts to occur after the flow is blocked back by the second gate at the downstream. The existence of the steady-state interaction between the weak and strong oblique shocks may be regarded as the third type of solution for the supercritical granular free-surface flow around a wedge since it can be generated both in the experiment and simulation by only changing the opening time of the second gate, while other conditions remain unchanged from generating the strong oblique shock.

Since there are much sharper jumps in flow properties across the strong oblique shock wave, the bulk inertial number becomes extremely small in the strong shock area, which might suggest that the underlying rheological behaviours of the material have changed. However, the work in this paper shows that the classic Coulomb friction law can still allow the solutions of the numerical simulation to be well agreed with the experiment.

The phenomena related to the granular strong shocks may also be important in applications. For example, if a strong shock wave could be triggered by controlling certain downstream infrastructures at an appropriate location, the damage of the natural hazardous flow would be alleviated to a controllable scale. Also, strong shocks may often occur in industrial processes, e.g., when paddy rice is poured into a rice milling chamber, a strong shock can be generated immediately once the grains impact the bottom of the vessel. Since the outlet conditions in such a container also need to be controlled in order to achieve for a better milling quality, a type of two-gate mechanism might bear certain analogy to the settings in this paper.

It might be useful to suggest a few areas that could be worked on in the future. The first area would be the conduct of the experiment in a broader range of control parameters in order to provide a more comprehensive evaluation to the settings of the two-gate system. For example, if the wedge angle becomes larger, the outflow conditions of the second gate may start to vary more substantially because the downstream flow has a greater two-dimensionality, and this may cause further deviations in gate height and opening time. Other interesting parameters, such as the moving rate of the shock intersection point, might also be worth a further attention, for example, to see if it could still be kept approximately con-

stant. On the other hand, adaptive mesh or dynamics mesh could be very useful for studying the shock interaction details observed in the granular flow simulation, where features associated with the slip-line and the supercritical jet downstream of the oblique shock would be particularly interesting.

#### Acknowledgements

The author would like to acknowledge the support of the NERC grant NER/A/S/2003/00439 and the EPSRC grant GR/R753-4/01 to the laboratory work conducted

during the time of the experiment, and is grateful to the constructive interactions with Professor J.M.N.T. Gray during the time of the postdoctoral research. The author would also like to acknowledge the support of the Innovate UK grant BB/S020993, which allows him to complete the work.

#### Data Availability

The data that support the findings of this study are available from the corresponding author upon reasonable request.

- \* Electronic address: [x.cui@shu.ac.uk](mailto:x.cui@shu.ac.uk); ORCID: 0000-0003-0581-3468
- <sup>1</sup> H. Rouse, Fluid mechanics for hydraulic engineers, McGraw-Hill Book Co., Inc., New York, N. Y., 1st Ed., (1938).
  - <sup>2</sup> A. T. Ippen, Mechanics of supercritical flow, *Trans. ASCE*, **116**, 269-295 (1951).
  - <sup>3</sup> J. J. Stoker, Water waves, *Interscience*, (1957).
  - <sup>4</sup> S. B. Savage, Gravity flow of cohesionless granular materials in chutes and channels, *J. Fluid Mech.* **92**, 53-96 (1979).
  - <sup>5</sup> S. B. Savage and K. Hutter, The motion of a finite mass of granular material down a rough incline, *J. Fluid Mech.* **199**, 177-215 (1989).
  - <sup>6</sup> K. Hutter, M. Siegel, S. B. Savage and Y. Nohguchi, Two-dimensional spreading of granular avalanche down an inclined plane. Part I: Theory, *Acta Mech.* **100**, 37-68 (1993).
  - <sup>7</sup> M. Wieland, J. M. N. T. Gray and K. Hutter, Channelised free surface flow of cohesionless granular avalanches in a chute with shallow lateral curvature, *J. Fluid Mech.* **392**, 73-100 (1999).
  - <sup>8</sup> J. M. N. T. Gray, Y. -C. Tai, and S. Noelle, Shock waves, dead-zones and particle-free regions in rapid granular free surface flows, *J. Fluid Mech.* **491**, 161-181 (2003).
  - <sup>9</sup> O. Pouliquen, Scaling laws in granular flows down rough inclined planes, *Phys. Fluids* **11**(3), 542-548 (1999a).
  - <sup>10</sup> O. Pouliquen, On the shape of granular fronts down rough inclined planes, *Phys. Fluids* **11**(7), 1956-1958 (1999b).
  - <sup>11</sup> O. Pouliquen and Y. Forterre, Friction law for dense granular flows: application to the motion of a mass down a rough inclined plane, *J. Fluid Mech.* **453**, 133-151 (2002).
  - <sup>12</sup> GDR Midi, On dense granular flows, *The European Phys. J. E* **14**, 341-365 (2004).
  - <sup>13</sup> P. Jop, Y. Forterre and O. Pouliquen, Crucial role of side-walls in granular surface flows: consequences for the rheology, *J. Fluid Mech.* **541**, 167-192 (2005).
  - <sup>14</sup> P. Jop, Y. Forterre and O. Pouliquen, A constitutive law dense granular flows, *Nature* **441**, 727-730 (2006).
  - <sup>15</sup> Y. Forterre, Kapiza waves as a test for three-dimensional granular flow rheology, *J. Fluid Mech.* **563**, 123-132 (2006).
  - <sup>16</sup> P.-Y. Lagr  e, L. Staron and S. Popinet, The granular column collapse as a continuum: validity of a two-dimensional Navier-Stokes model with a  $\mu(I)$ -rheology, *J. Fluid Mech.* **686**, 378-408 (2011).
  - <sup>17</sup> L. Staron, P.-Y. Lagr  e and S. Popinet, The granular silo as a continuum plastic flow: the hour-glass vs the clepsydra,

- Phys. Fluid* **24**, 103301 (2012).
- <sup>18</sup> A. Holyoake and J. N. McElwain, High-speed granular chute flows, *J. Fluid Mech.* **710**, 35-71 (2012).
- <sup>19</sup> J. M. N. T. Gray and A. N. Edwards, A depth-averaged  $\mu(I)$ -rheology for shallow granular free-surface flows, *J. Fluid Mech.* **755**, 503-534 (2014).
- <sup>20</sup> T. Barker<sup>1</sup>, D. G. Schaeffer, P. Bohorquez and J. M. N. T. Gray, Well-posed and ill-posed behaviour of the  $\mu(I)$ -rheology for granular flow, *J. Fluid Mech.* **779**, 794-818 (2015).
- <sup>21</sup> J. D. Goddard and J. Lee, On the stability of the  $\mu(I)$  rheology for granular flow, *J. Fluid Mech.* **833**, 302-331 (2017).
- <sup>22</sup> M. Trulsson, Rheology and shear jamming of frictional ellipsoids, *J. Fluid Mech.* **849**, 718-740 (2018).
- <sup>23</sup> D. Nagy, P. Claudin, T. B  rzs  nyi and E. Somfai, Flow and rheology of frictional elongated grains, *New J. Phys.* **22**, 073008 (2020).
- <sup>24</sup> H. Ma and Y. Zhao, Investigating the flow of rod-like particles in a horizontal rotating drum using DEM simulation, *Granular Matter* **22**:41 (2018).
- <sup>25</sup> Y. Liu, Z. Yu, J. Yang, C. Wassgren, J. S. Curtis and Y. Guo, Discrete element method investigation of binary granular flows with different particle shapes, *Energies* **13**, 1841 (2020).
- <sup>26</sup> Y. Zhu, R. Delannay and A. Valance, High-speed confined granular flows down smooth inclines: scaling and wall friction laws,  $\mu(I)$  rheology for granular flow, *Granular Matter* **22**:88 (2020).
- <sup>27</sup> E. D. Fern  ndez-Nieto, J. Garres-D b, A. Mangeney and G. Narbona-Reina, 2D granular flows with the  $\mu(I)$  rheology and side walls friction: A well-balanced multilayer discretization, *J. Comput. Phys.* **356**, 192-219 (2018).
- <sup>28</sup> A. Franci and M. Cremonesi, 3D regularized  $\mu(I)$ -rheology for granular flows simulation, *J. Comput. Phys.* **378**, 257-277 (2019).
- <sup>29</sup> Y. -C. Tai, S. Neolle, J. M. N. T. Gray, and K. Hutter, Shock-capturing and front-tracking methods for granular avalanches, *J. Comput. Phys.* **175**, 269-301 (2002).
- <sup>30</sup> E. B. Pitman, C. C. Nichita, A. Patra, A. Bauer, M. Sheridan and M. Bursik, Computing granular avalanches and landslides, *Phys. Fluids* **15**(12), 3638-3646 (2003).
- <sup>31</sup> K. M. H  konard  ttir and A. J. Hogg, Oblique shocks in rapid granular flows, *Phys. Fluids* **17**, 0077101 (2005).
- <sup>32</sup> Y. Amarouchene and H. Kelly, Speed of sound from shock

This is the author's peer reviewed, accepted manuscript. However, the online version of record will be different from this version once it has been copyedited and typeset.

PLEASE CITE THIS ARTICLE AS DOI: 10.1063/1.50057700

- fronts in granular flows, *Phys. Fluids* **18**, 031707 (2006).
- <sup>33</sup> J. M. N. T. Gray and X. Cui, Weak, strong and detached oblique shocks in gravity-driven granular free-surface flows, *J. Fluid Mech.* **579**, 113-136 (2007).
- <sup>34</sup> X. Cui, J. M. N. T. Gray and T. Jóhannesson, Deflecting dams and the formation of oblique shocks in snow avalanches at Flateyri, Iceland, *J. Geophys. Res.* **112**, F04012 (2007).
- <sup>35</sup> C. G. Johnson and J. M. N. T. Gray, Granular jets and hydraulic jumps on an inclined plane, *J. Fluid Mech.* **675**, 87-116 (2011).
- <sup>36</sup> X. Cui and J. M. N. T. Gray, Gravity-driven granular free-surface flow around a circular cylinder, *J. Fluid Mech.* **720**, 314-337 (2013).
- <sup>37</sup> S. Viroulet, J. L. Baker, A. N. Edwards, C. G. Johnson, C. Gjaltema, P. Clavel and J. M. N. T. Gray, Multiple solutions for granular flow over a smooth two-dimensional bump, *J. Fluid Mech.* **815**, 77-116 (2017).
- <sup>38</sup> Delannay, R., Valance, A., Mangeney, A., Roche, O. and P. Richard, Granular and particle-laden flows: from laboratory experiments to field observations, *J. Phys. D.* **50**, 053001 (2017).
- <sup>39</sup> S. S. Grigorian, M. E. Eglit, and Iu. L. Iakimov, New state and solution of the problem of the motion of snow avalanche. *Snow, Avalanches & Glaciers. Tr. Vysokogornogo Geofizich Inst.* **12**, 104-113 (1967).
- <sup>40</sup> A. G. Kulikovskii and M. E. Eglit, Two-dimensional problem of the motion of a snow avalanche along a slope with smoothly changing properties, *J. Appl. Maths Mech.* **37(5)**, 792-803 (1973).
- <sup>41</sup> M. E. Eglit, Some mathematical models of snow avalanches, in "Advances in mechanics and the flow of granular materials" (ed. M. Shahinpoor), Clausthal-Zellerfeld and Gulf Publishing Company, **2**, 577-588 (1983).
- <sup>42</sup> S. B. Savage and K. Hutter, The dynamics of avalanches of granular materials from initiation to run-out. Part I: Analysis, *Acta Mechanica.* **86**, 201-203 (1991).
- <sup>43</sup> R. Greve and K. Hutter, Motion of a granular avalanche in a convex and concave curved chute: experiments and theoretical predictions, *Phil. Trans. R. Soc. Lond. A* **342**, 573-600 (1993).
- <sup>44</sup> J. M. N. T. Gray, M. Wieland and K. Hutter, Free surface flow of cohesionless granular avalanches over complex basal topography, *Proc. Roy. Soc. A* **455**, 1841-1874 (1999).
- <sup>45</sup> A. Harten, High resolution schemes for hyperbolic conservation laws, *J. Comput. Phys.* **49**, 357-393 (1983).
- <sup>46</sup> H. Nessyahu and E. Tadmor, Non-oscillatory central differencing for hyperbolic conservation laws, *J. Comput. Phys.* **87**, 408-463 (1990).
- <sup>47</sup> G. -S. Jiang, D. Levy, C. -T. Lin, S. Osher, and E. Tadmor, High-resolution nonoscillatory central schemes with nonstaggered grids for hyperbolic conservation laws, *SIAM J. Numer. Anal.* **35**, 2147-2168 (1998).
- <sup>48</sup> A. Kurganov and E. Tadmor, New high-resolution semi-discrete central schemes for Hamilton-Jacobi Equations, *J. Comput. Phys.* **160**, 720-742 (2000).
- <sup>49</sup> Y. -J. Liu, Central schemes on overlapping cells, *J. Comput. Phys.* **209**, 82-104 (2005).
- <sup>50</sup> G. Tóth, D. Odstrčil, Comparison of some flux corrected transport and total variation diminishing numerical schemes for hydrodynamic and magneto-hydrodynamic problems, *J. Comput. Phys.* **128**, 82-100 (1996).
- <sup>51</sup> X. Cui, Computational and experimental studies of rapid granular free-surface flows around obstacles, *Computers & Fluids* **89**, 179-190 (2014).
- <sup>52</sup> J. D. Anderson Jr., Computational fluid dynamics, McGraw-Hill Education (1995).
- <sup>53</sup> G. -S. Jiang, D. Levy, C. -T. Lin, S. Osher and E. Tadmor, High-resolution nonoscillatory central schemes with non-staggered grids for hyperbolic conservation laws, *SIAM J. Numer. Anal.* **35**, 2147-2168 (1998).
- <sup>54</sup> B. Edney, Anomalous heat transfer and pressure distributions on blunt bodies at hypersonic speeds in the presence of an impinging shock, Aeronautical Research Institute of Sweden, Report 115, Stockholm (1968).
- <sup>55</sup> F. Grasso, C. Purpura, B. Chancetz and J. Déclery, Type III and type IV shock/shock interferences: theoretical and experimental aspects, *Aerospace Science & Technology*, 93-106, (2003).